



# Study of the influence of additive manufacturing applicable surface treatment methods on mechanical part properties for use in aerospace applications

Christin Rümmler<sup>1</sup> · Gregor R. H. Neumann<sup>1</sup> · Wolfram Groh<sup>1</sup> · Falk Hähnel<sup>1</sup> · Gundis Grumbt<sup>2</sup> · René Tropeschuh<sup>3</sup> · Tom Schiemann<sup>2</sup> · Johannes F. C. Markmiller<sup>1</sup>

Received: 23 June 2023 / Revised: 25 January 2024 / Accepted: 30 January 2024 / Published online: 9 March 2024  
© The Author(s) 2024

## Abstract

The adequate assessment of the quality of parts produced by additive manufacturing is crucial for their application in the aviation industry. Therefore, parameters of the manufacturing process, which influence the part quality, have to be identified and quantified to reveal existing correlations. Besides, it is essential to gain an overall understanding of the influence of each step in the additive manufacturing chain, including also post-process treatments and inspection methods, on the data, which is used to develop a statement about the additively manufactured parts' quality. The present study aims on forming such a comprehensive picture. For this purpose, 120 test specimens from AISi10Mg were manufactured on an EOS M 290. Four different surface treatments (centrifugal blasting, barrel finishing, abrasive flow machining and turning & polishing) were applied to the specimens and compared to the as-built condition regarding the resulting material properties. The relative density, surface roughness, surface hardness, ultimate tensile strength, yield strength, Young's modulus and the fatigue properties were determined and analysed especially for correlations with the surface treatment and specimen positions in the build space. The surface roughness, fatigue properties and static tensile properties showed to be dependent on the applied surface treatment, while fewer correlations could be found regarding the surface hardness and relative part density. No clear indication was found relating one of the mentioned properties to certain areas in the build space.

**Keywords** Additive manufacturing · Surface treatment · Part quality · Aerospace qualification · Laser powder bed fusion

## 1 Introduction

An ongoing and increasing interest in additive manufactured (AM) parts can be observed in various industries. In the aviation sector, a number of different parts have been brought into service. Examples are the A350 door latch shaft [1] or the A380 hydraulic block [2]. Critical to part qualification and process certification is the dependency of part properties on the material used and the manufacturing process, which in turn depends on the type of utilised

machine, the manufacturing parameters and again on the raw material and its quality [3]. These circumstances result in complex and tedious qualification and certification processes for AM materials, parts and manufacturing processes in the aviation industry, since an exhaustive and comprehensive knowledge of the involved processes and their influence of the part's final quality must be demonstrated. This extends to all steps of the manufacturing process: the raw material and its supply, the printing process itself and often multiple post-process steps, like heat treatment, hot isostatic pressing, surface treatment or processing. Each step entails parameters which are critical to part quality and therefore, need to be identified in the qualification process. A tolerance band has to be established for each key process variable afterwards and compliance throughout the process must be demonstrated, that the established limits are met. However, there are no comprehensive studies available to the broad expert audience to generate the necessary general understanding of the influence of parameters of the manufacturing

---

✉ Christin Rümmler  
christin.ruemmler@tu-dresden.de

<sup>1</sup> Institute of Aerospace Engineering, Technische Universität Dresden, 01062 Dresden, Germany

<sup>2</sup> IMA Materialforschung und Anwendungstechnik GmbH Dresden, 01109 Dresden, Germany

<sup>3</sup> AM Metals GmbH, 09633 Halsbrücke, Germany

chain on key properties, which are currently used to assess the components' quality. Therefore, this study focuses on generating information on a sound data basis to allow for overall conclusions. The aim was set to cover the holistic AM manufacturing process from the powder, the printing process, followed by surface treatment to non-destructive and destructive inspections. Special emphasis was put on investigating the influence of mechanical surface treatment on the mechanical properties, which are used to assess the quality of parts produced by laser powder bed fusion (LPBF).

During the LPBF process, powder is locally melted through a laser beam. First, a thin layer of powder is spread over the build tray. The laser melts the powder particles along a predefined path. As soon as the exposure of one powder bed layer is completed, the platform is lowered by the layer thickness and the next layer is created by a recoater distributing powder from a powder reservoir. That way, the solidified material creates the final part layer by layer. The whole LPBF process takes place in an inert gas atmosphere. Detailed descriptions of the method may be found in [4, 5].

A post-process treatment of the manufactured parts is necessary for many applications to eliminate defects or favour certain properties. Several research has been conducted on the impact of different surface and heat treatment methods on AM parts. Kim et al. investigated the characteristics of 304 L stainless steel specimens treated with conventional machining and induction-assisted machining [6]. The surface characteristics after the post-processing operations finish machining, vibratory surface finishing and drag finishing were highlighted by Kaynak et al. [7]. For AlSi10Mg, Tradowsky et al. investigated the impact of thermal post-processing, Hot Isostatic Pressing, T6-peak ageing treatment and post-process machining on the microstructural and mechanical properties development [8]. The effect of heat treatment on mechanical properties for AlSi10Mg specimens was also analysed by Hitzler et al. [9] and Kempen et al. [10]. Furthermore, Sun et al. investigated the influence of the as-built surface of selective electron beam melted Ti-6Al-4V specimens on their tensile properties [11]. The effect of sandblasting and turning on 316 L stainless steel shells was analysed by Mehta et al. [12], who also examined the microstructure and surface roughness of these specimens.

In addition, there are extensive reviews given by several authors on the topic of different AM post-processing operations and their impact on certain microstructural or mechanical properties or part quality [13–16]. Furthermore, Pal and Basak [17] give an overall review on the links between powder properties, printing parameters, post-processes and fatigue properties for AlSi10Mg. However, it is difficult to gain a whole set of information, beginning at the powder characteristics over manufacturing steps to

multiple inspections, to draw final conclusions between various methods of treatment, as mentioned in the beginning of this introduction.

The present study focuses on the effect of AM surface treatment methods in the metal AM rapid prototyping industry, which can be applied to parts of various dimensions and geometries. Five different surface conditions were compared in the present study. The as-built (AB) condition was established as a first reference, which was expected to have the strongest influence on the material properties. To have a second reference with the least impact of surface quality, the processes turning and polishing (TP) were selected. The other three treatments are typical AM surface finishes for prototyping: centrifugal blasting (CB), abrasive flow machining (AFM) and barrel finishing (BF). To gain a wide picture of the mechanical part properties after those treatments, the following properties were evaluated: surface roughness, part density, surface hardness, ultimate tensile strength, yield strength, Young's modulus and fatigue resistance.

## 2 Experimental procedure

### 2.1 General overview

The experimental investigations are divided into a number of individual steps, which are listed in Table 1. In the first step, for the sake of data set completeness, the powder material was analysed to obtain data of the raw material. In step two, the test specimens were fabricated. In steps three and four, the geometry and surface properties of the test specimens were determined directly after the build process. This initial obtained data was the basis for evaluating the effects of the surface treatment processes used in step five. During steps

**Table 1** Steps of the experimental investigation procedure

Step	Description
1	Powder analysis
2	Manufacturing on an EOS M 290 metal 3D printer
3	Surface roughness measurement
4	Geometry scan
5	Surface treatment
6	Surface roughness measurement
7	Geometry scan
8	Density measurement
9	Thread cutting
10	Geometry scan
11	Static tensile/fatigue test
12	Hardness measurement

six and seven, the geometry and surface properties were determined again on the processed samples. In step eight the density measurement of the specimens was conducted. Afterwards in step nine, the test specimens were prepared for further testing. To detect a possible influence of the thread cutting, the geometry of the test specimens was determined once more in step ten. Finally, in steps eleven and twelve, important mechanical properties of the specimens were determined to deduce the influence of the surface treatment processes.

## 2.2 Test specimen specifications

The surface constitution of components influences a wide range of properties. To determine the mechanical behaviour, which is the focus in this study, tests must be carried out under both static and dynamic (fatigue) loading. The dimensions of the specimens for the static tests are determined according to DIN EN ISO 6892-1 and those for the fatigue tests according to DIN EN 6072 as illustrated in Fig. 1.

For reasons of comparability of the specimens after surface treatment, the diameters of the specimens in the test area were adjusted according to the expected material removal through each treatment, which are listed in Table 2. In addition, it was determined that for each surface condition 12 specimens would be prepared for static tensile tests (referred to as S-specimens) and 12 specimens for fatigue tensile tests (referred to as F-specimens). Thus, a total of 120 test specimens were required in the study.

The samples were designed with an unique specimen identifier, which was engraved in the top and bottom part of each test sample. It consisted of an abbreviation for the surface treatment method (AB, CB, BF, AFM or TP), as well as the type of specimen (S for static tensile tests or F for fatigue tests) and finally a consecutive number from 1 to 60. For example CB-S14 was the 14th static tensile test

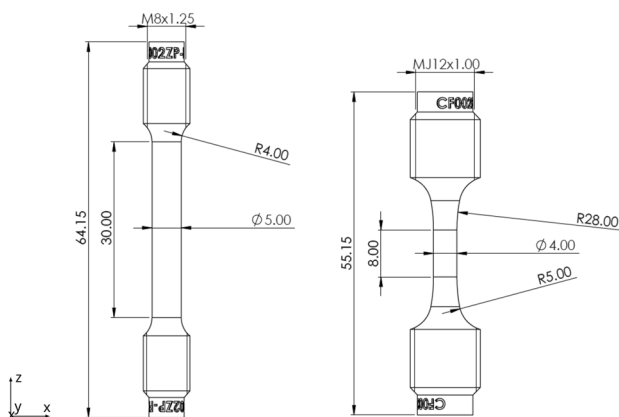


**Fig. 1** Specimen dimensions for static tensile tests (left) and fatigue tests (right), all dimensions in mm

**Table 2** Diameters of the specimens' test area, adjusted according to expected material removal during surface treatment

Surface treatment category	S-specimens diameter (mm)	F-specimens diameter (mm)
According to standard	5.00	4.00
As-built	5.00	4.00
Centrifugal blasting	5.50	4.50
barrel finishing	5.30	4.30
Abrasive flow machining	5.30	4.30
Turning and polishing	7.00	6.00

specimen and has been treated with centrifugal blasting, whereas TP-F60 has been turned and polished and was the 60th fatigue test specimen.

## 2.3 Material and specimen manufacturing process

The test specimens were produced from the material AlSi10Mg on an EOS M 290 machine. One lot of AlSi10Mg was used for the print job. Powder properties, which have been labelled as crucial on the final part quality in other published work [18, 19], were analysed and are summarised in Table 3.

The EOS M 290 was equipped with an Online Tomography and a Powder Bed Monitoring System. The print parameters were chosen based on literature research and are summarised in Table 4. They do not equal the recommended EOS-set of parameters for this material. However, resulting non-optimal end properties were acceptable since the objective of the study was to compare different surface treatment methods.

All 120 specimens were produced in one print job. The positioning of the specimens on the build tray and the assignment to the post-processes are presented in Fig. 2. Specimens of the same configuration, according to the planned surface finish, were arranged almost linearly on the build tray. The recoater moved along the rows, while the shielding gas flow was conducted along the columns, as shown in Fig. 2. The specimens were not positioned in parallel to the recoater axis to reduce the risk of contact with the recoater blade during the application of fresh powder layers. No support structure was required for the fabrication of the specimens. Finally, 12 pairs of specimens, consisting of one S- and one F-specimen, for each surface finish, were obtained. The positions of the individual specimen pairs were taken into account in all subsequent examinations. It is important to notice that the S-specimens were placed in rows with odd numbers and all F-specimens in even ones.

After the print job was completed, the loose powder was removed and the specimens, which were still fixed on the plate, were briefly manually sandblasted to remove attached

**Table 3** Powder characteristics of the processed AlSi10Mg powder

Characteristic	Result	Test method	Test standard
PSD <sup>1</sup>			
d10	27.871 $\mu\text{m}$	Laser diffraction	ISO13320-1
d50	47.503 $\mu\text{m}$		
d90	79.117 $\mu\text{m}$		
Bulk density	4.01 $\text{g}/\text{cm}^3$	Hall funnel	DIN EN ISO 3923-1 <sup>2</sup>
Flowability	9 s/50 g	Hall funnel	DIN EN ISO 4490 <sup>2</sup>
Oxygen content	0.065%	Infrared absorption <sup>3</sup>	DIN 54387-3
Nitrogen content	<0.0015%	Thermal conductivity <sup>3</sup>	DIN 54387-3
Hydrogen content	<0.005%	Infrared absorption <sup>3</sup>	–
Chemical analysis			
Al	89.32%	XRF spectroscopy <sup>4</sup>	–
Si	9.58%		
Fe	0.45%		
Mg	0.31%		
Cu	0.21%		
Cr	0.04%		
Ti	0.03%		
Mn	0.03%		
Zr	0.02%		
Ga	99 ppm		

<sup>1</sup>Powder size distribution

<sup>2</sup>Flow opening diameter: 5 mm

<sup>3</sup>The analysis was conducted with a LECO ONH836

<sup>4</sup>The analysis was conducted with a Bruker Tiger S8

**Table 4** Manufacturing parameters

Parameter	Value
Inert gas	Argon
Recoating speed	150 mm/s
Differential pressure	0.38 mbar
Laser power	370 W
Laser speed	1300 mm/s
Hatch distance	0.19 mm
Energy input	37.45 $\text{J}/\text{mm}^3$
Layer thickness	40 $\mu\text{m}$
Skywriting	On
Hatch rotation angle	67°
Platform temperature	35°C

particles. Thereafter, the specimens were cut off the build tray and ran through the inspection processes as described in Sect. 2.1 and Table 1, respectively.

## 2.4 Surface finishes

The surface treatments under consideration can achieve considerably different surface qualities depending on how they are carried out and the parameters chosen. The selection of

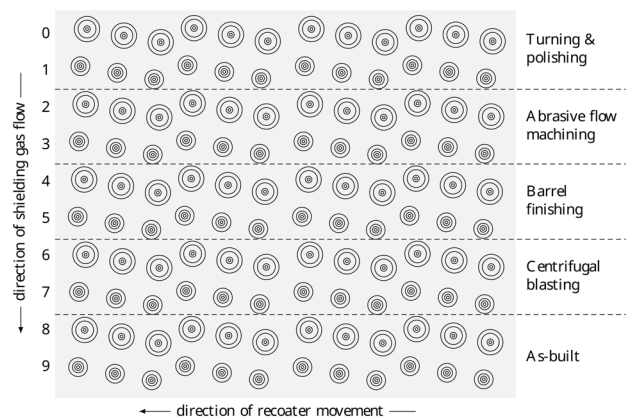


**Fig. 2** Top view of the arrangement of specimens on the build tray and assignment of applied surface treatments

the parameters listed in the following subsections is based on the experience of the contracted manufacturer.

### 2.4.1 As-built condition

Test specimens, which are further referenced in “as-built” condition, have not been surface nor heat treated.

### 2.4.2 Turning and polishing

The specimens of this finish category were conventionally turned and polished afterwards, which resulted in a removal of 1 mm of thickness relative to the original surface.

### 2.4.3 Centrifugal blasting

The centrifugal blasting of the specimens was performed in an automated process using a stainless steel abrasive (Cronital). The finish was applied in two steps: first, the centrifugal blasting machine ran at 9000 rpm for 5 min and second, at 7000 rpm for another 5 min. An average diameter reduction along the test cross section was derived based on the 3D scans of the specimens before and after the surface treatment. Material with a thickness in the range of 10–30  $\mu\text{m}$  was removed from the surface by centrifugal blasting.

### 2.4.4 Barrel finishing

The resulting surface quality and the amount of removed material of barrel finished parts is highly dependent on certain factors: the choice of abrasives, in terms of material, surface roughness and geometry; the surface orientation of the work item, meaning internal or external surface; the ratio of part volume to abrasive volume as well as the processing time [20]. For the experimental setup of this study, the BF consisted of three sub-steps. First, polyhedral ceramic abrasives at a barrel speed of 50 rpm were used to achieve a coarse finish over 60 min. Second, pyramidal ceramic abrasives at a barrel speed of 300 rpm over 90 min were applied to achieve a strong abrasion. Third, and finally, a polished surface is generated by the usage of cylindrical ceramic abrasives for 30 min at a barrel speed of 300 rpm. By this surface treatment, a reduction in diameter by 40–60  $\mu\text{m}$  was observed.

### 2.4.5 Abrasive flow machining

Detailed information of this treatment method can be found in [21]. The predetermined specimens were mounted in groups of four in a specially designed holder in a container, through which the flowing abrasive was conducted forcefully. An adequate design of the mounting, which has been adapted to part geometry, is crucial for the procedure, because it influences the resulting flow velocity and hence the pressure leading to abrasion. The treatment for the static test specimens lasted for 112 min at 30 bar using a medium abrasive paste and 47 min at 25 bar with a fine-grained abrasive. The fatigue specimens were treated at 35 bar for 95 min with the medium abrasive and at 25 bar for 47 min in a second session with the fine-grained abrasive paste. Detailed information regarding the abrasives

could not be obtained due to a non-disclosure notice by the manufacturer. 270  $\mu\text{m}$  up to 740  $\mu\text{m}$  of material were removed with this treatment.

## 3 Property determination, results and discussion

The following results of the investigation are often presented in the form of heat maps. This way, the obtained properties of specimens placed on the build tray at certain locations (see Fig. 2, top view of the build tray) are visualised by colour-coded squares. This form of presentation allows for a fast assessment whether the mapped property is dependent on the position on the build tray or not. It is important to notice that the specimens for static tensile test were placed in rows with odd numbers and all specimens for fatigue tests in even ones. Specimens placed in the same row were equally surface treated.

Furthermore, it must be noted that properties of AM parts vary with their orientation of build, which is described more in detail in [22–24]. Therefore, an investigation of the influence of the orientation of build was not of interest to this study and all specimens were placed vertically. However, if references from other publications are used in the following discussion, it was ensured that only results from specimens with vertical orientation were adduced.

If not declared otherwise, the uncertainty of the mean in the following sections was determined in accordance with reference [25]. It states that the uncertainty  $u$  for the arithmetic mean  $q$  of a random variable, for which  $n$  independent observations have been obtained, can be estimated with the standard deviation of the mean  $s(q)$  with Eq. 1 (Type A evaluation of standard uncertainty).

$$u = k \frac{s(q)}{\sqrt{n}}. \quad (1)$$

A coverage factor  $k$  might be chosen that corresponds to a particular level of confidence, which was chosen to be  $k = 2$  leading to an interval having a 95% level of confidence.

### 3.1 Surface roughness

Two different inspection methods were applied to determine the test specimens' surface roughness: a tactile measuring system Mahr Perthometer Concept and the Keyence VR-3000, an optical measuring system in compliance with DIN EN ISO 4287. The tactile measurement was conducted based on DIN EN ISO 4287 / DIN EN ISO 3274 as well.

### 3.1.1 Tactile measurement

The tactile measurement device was equipped with a tip with a radius of 2  $\mu\text{m}$ . Furthermore, the test length was set to 4.0 mm according to the standard DIN EN ISO 4287 with reference to the TP-specimens. Furthermore, a corresponding cut-off wavelength of  $\lambda_c = 0.8 \text{ mm}$  was selected.

The results for the average roughness  $Ra$  and the mean roughness depth  $Rz$  for 115 of the 120 specimens determined with the tactile measuring system are displayed in Figs. 3 and 4. Each square represents one roughness value of the specimen, which has been positioned at this spot during the manufacturing process (top view). The systematic uncertainty for  $Ra_{\text{tac}}$  amounts to 6.3% and for  $Rz_{\text{tac}}$  to 6.0% according to the latest calibration certificate. Light grey squares indicate that no valid measurements were taken from these samples, due to minor issues during the data collection process. This affected the specimens CB-S22, CB-F24, BF-F27, BF-F28 and BF-F36.

The results are summarised in Table 5 as well, where the combined uncertainties (systematic and statistical) for the determined means are given. It is evident, that varying surface qualities were achieved by the applied surface finish. In the as-built condition, the highest values of surface roughness were measured, which are comparable to values that can be found in other publications:  $Ra \approx 12 \mu\text{m}$  [4],  $Ra \approx 13 \mu\text{m}$  [26] or  $Ra \approx 10 \mu\text{m}$  to  $40 \mu\text{m}$  [27].

The highest surface quality was achieved with the processes TP, which fits the expectations since 1 mm of material was mechanically removed. It is likely that AM specific defects present in the surface layer were completely eliminated by this process.

CB created a smoother surface compared to the as-built samples, but still remarkably high values of surface roughness were measured.

BF and AFM delivered surface conditions comparable to each other. However, the uncertainty for  $Ra_{\text{BF}}$  and  $Rz_{\text{BF}}$  were

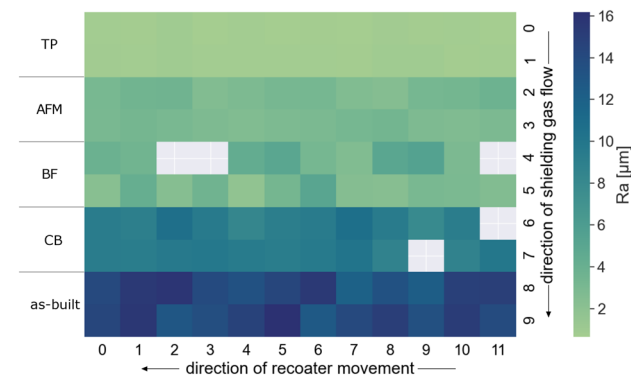


**Fig. 3** Average roughness  $Ra$  for 115 of 120 test specimens in post-processed condition, data generated by tactile measurement

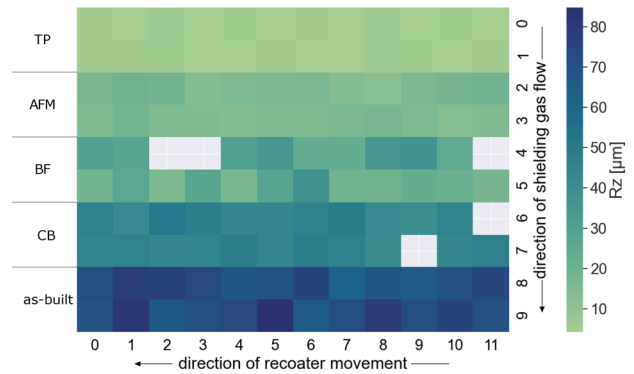


**Fig. 4** Mean roughness depth  $Rz$  for 115 of 120 test specimens in post-processed condition, data generated by tactile measurement

twice as high as  $Ra_{\text{AFM}}$  and  $Rz_{\text{AFM}}$ . This originated from an increased scattering of the test specimens'  $Ra_{\text{BF}}$  and  $Rz_{\text{BF}}$  values resulting in an increased standard deviation. Nevertheless, one has to take into account that a longer process time during BF might have led to a lower surface roughness, but it is also possible that a convergence was already reached, as described by Boschetto et al. [20].

### 3.1.2 Optical measurement

According to the manufacturer specifications, the repeat accuracy as a measure of uncertainty was given to be  $\pm 0.5 \mu\text{m}$  for the used device Keyence VR-3000. The optical measurement of surface roughness could only be performed on a smaller portion of the 120 samples. Four test specimens per finish category before and after the treatment were examined. Therefore, the statistics derived by this investigation should be mostly considered as an indication. For the optical measurements a  $\lambda_c = 8.0 \text{ mm}$  was used with the exception of a  $\lambda_c = 2.5 \text{ mm}$  for the TP-specimens.

**Table 5** Results for the average roughness  $Ra$ , the mean roughness depth  $Rz$  derived by tactile measurement and the Brinell hardness per post-process and specimen category (S-static tensile, F-fatigue), combined uncertainty (systematic and statistical) is given

Row	$Ra$ ( $\mu\text{m}$ )	$Rz$ ( $\mu\text{m}$ )	HBW 2.5/62.5	Finish
0	$0.76 \pm 0.09$	$4.8 \pm 0.6$	$135.4 \pm 5.1$	TP (S)
1	$0.83 \pm 0.08$	$4.8 \pm 0.4$	$134.5 \pm 6.2$	TP (F)
2	$3.1 \pm 0.4$	$16.4 \pm 2.4$	$136.2 \pm 5.4$	AFM (S)
3	$3.0 \pm 0.3$	$15.4 \pm 1.8$	$133.1 \pm 5.7$	AFM (F)
4	$4.0 \pm 0.7$	$29.9 \pm 4.3$	$136.6 \pm 5.2$	BF (S)
5	$3.0 \pm 0.7$	$23.0 \pm 4.9$	$133.2 \pm 5.5$	BF (F)
6	$9.4 \pm 1.0$	$45.5 \pm 4.5$	$136.4 \pm 5.4$	CB (S)
7	$9.5 \pm 0.9$	$45.6 \pm 3.9$	$134.4 \pm 6.0$	CB (F)
8	$14.2 \pm 1.6$	$71.5 \pm 7.0$	$136.3 \pm 5.1$	As-built (S)
9	$14.4 \pm 1.5$	$73.7 \pm 7.7$	$131.2 \pm 5.5$	As-built (F)

The characteristic values for each specimen were based on 31 sampling lengths. The results for the derived  $Ra$  values before and after the surface treatment are displayed in Fig. 5. The samples AB-F1, AB-F2, AB-S1 and AB-S2 remained in the as-built condition.

### 3.1.3 Comparison of tactile and optical surface roughness inspection methods

Generally, the qualitative results derived from the tactile measurement can be confirmed with the optical measurement. However, the absolute values deviated significantly from those obtained with the tactile measurement system. To investigate this discrepancy, a comparison of the tactile and the optical method for the same specimens in equal finish conditions is presented in Fig. 6.  $Ra_{opt}$  mean values were observed to be two times higher across all finish categories than  $Ra_{tac}$ .

Comparisons of tactile and optical roughness measurement methods have already been conducted, but were mostly based on surfaces of conventionally manufactured components [28, 29]. Bernevig-Sava et al. stated that the tactilely measured profiles of sandblasted AM specimens contain errors, due to sintered powder particles on the surface [30]. Cheng et al. described that optical and tactile methods can generate comparable values for the characterisation of AM surfaces, but the tip angle of tactile systems can affect the results for  $Rz$  [31].

Generally, the used Mahr Perthometer Concept (tactile, see Sect. 3.1.1) and the Keyence VR-3000 (optical, see Sect. 3.1.2) were both capable of determining roughness parameters using internal algorithms. The tactile system did not allow to deviate the profile length and evaluation parameters from the standard (Operating Instructions Perthometer Concept, Mahr GmbH, Göttingen, 2002). Furthermore, the tactile measurement length was limited to a maximum of 20 mm.

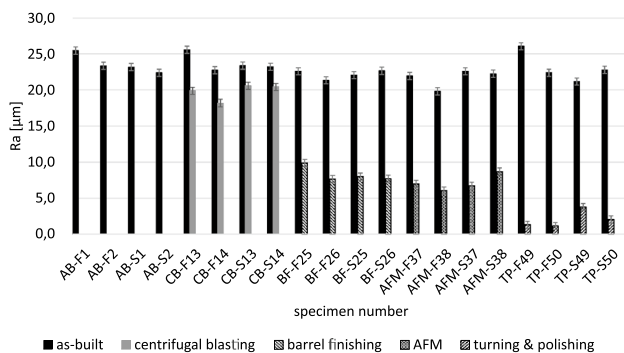


**Fig. 5** Average roughness  $Ra$  for a selection of specimens in the as-built (before) and in the finished condition (after) derived by optical measurement

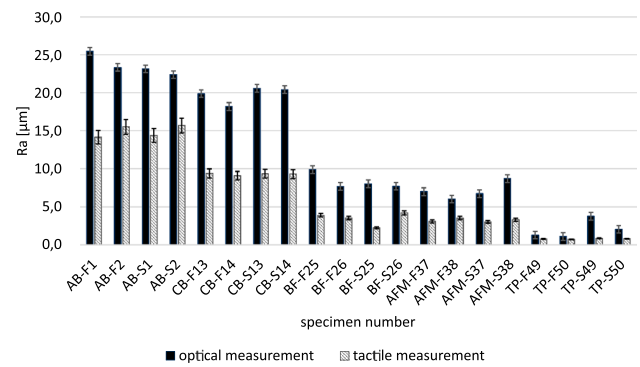


**Fig. 6** Comparison of  $Ra$  values determined by optical and tactile measurement

The boundary conditions for both measurement systems were identical, apart from the evaluated profile length and the cut-off wavelength  $\lambda_c$ . To investigate whether the origin of the deviation lied within these two parameters, a short experiment was conducted on five identical bar-shaped test specimens fabricated from AISi10Mg and the same manufacturing parameters as described in Sect. 2.3. Altogether, a number of 220 profiles was scanned and evaluated on these specimens with the tactile and optical devices. 200 profiles with a length of 12.5mm and 20 profiles with a length of 4.0mm per method were evaluated in total. Additionally, 50 profiles with a length of 40.0mm were evaluated solely with the optical system, since the maximum measurement length of the tactile device was exceeded.

The profile parameters  $Ra$  and  $Rz$  were evaluated and inspected for all profiles for further analysis. Table 6 summarises the results of all 220 conducted measurements. No clear difference could be identified for the  $Ra$  values when comparing both inspection systems. However, an evident dependence of  $Ra$  on the length of the measuring distance was recognisable. The short profile lengths always resulted in significantly smaller values of  $Ra$  than increased test lengths. The profile parameter  $Rz$  showed a similar behaviour.

The differences between tactile and optical measurement for the as-built specimens of the main experimental setup of static and fatigue test specimens could be

**Table 6** Resulting roughness profile parameters  $Ra$  and  $Rz$  based on different test lengths, combined uncertainty (systematic and statistical) is given

Test length	40.0mm	12.5mm	4.0mm
$Ra_{tac}$ ( $\mu\text{m}$ )	–	$19.7 \pm 1.6$	$13.5 \pm 1.1$
$Ra_{opt}$ ( $\mu\text{m}$ )	$22.3 \pm 0.8$	$20.0 \pm 0.9$	$14.3 \pm 1.0$
$Rz_{tac}$ ( $\mu\text{m}$ )	–	$120.6 \pm 9.1$	$74.3 \pm 6.6$
$Rz_{opt}$ ( $\mu\text{m}$ )	$170.0 \pm 3.4$	$124.8 \pm 2.6$	$71.9 \pm 4.9$

reproduced comparing the 40.0 mm and the 4.0 mm test lengths on the bar-shaped specimens. Therefore, the values derived from optical measurement are considered to be representative for the specimens' surface roughness. However, the calculation of a general correction factor for different profile lengths cannot be realised, because the differences between the methods vary depending on the surface condition (see Fig. 6).

### 3.2 Surface hardness

The Brinell hardness test HBW was used to determine the specimens' surface hardness according to DIN EN ISO 6506-1:2015-02. A diameter of 2.5 mm was chosen for the indenter with a 62.5 kgf force, which equals 613.1 N, for 14 s using a ZwickRoell EMCOTEST Duravision 20G5. The uncertainty amounts to 4.6 HBW given in the device's calibration certificate. The measurement was conducted on the top surface of the specimens.

The measured hardness values showed slight variations across the different surface treatment categories, see Table 5. The derived hardness per finish category and specimen type (static/ fatigue) ranged from  $131.2 \pm 5.5$  HBW 2.5/62.5 (AB-F-specimens) to  $136.6 \pm 5.2$  HBW 2.5/62.5 (BF-S-specimens). These results are higher than the ones derived by Marchese et al. of  $104 \pm 1$  HBW 2.5/62.5 [32], but are in line with Padovano et al. [33].

However, the depiction of the distribution of the test specimens' hardness on the build tray, see Fig. 7, reveals that those specimens, which are furthest from the shielding gas source, appear to be in the lower range of the measured results. Furthermore, all F-specimens showed hardness values in the upper half of the observed range.

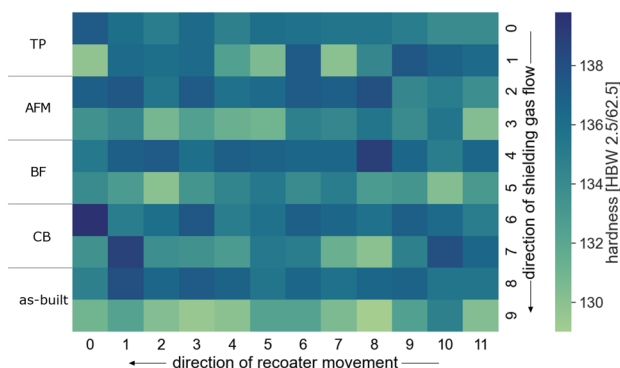


**Fig. 7** Hardness distribution over the platform for various surface finish conditions

### 3.3 Density

The density of all 120 specimens was determined by the Archimedes' method according to DIN EN ISO 3369:2010-08, using a Sartorius electrical analytical scale LA 230 S in combination with a Sartorius density determination set YDK 01. A systemic deviation cannot be indicated, since there is no accepted reference material, but the interval of reproducibility is given to be  $0.03 \text{ g/cm}^3$  [34].

For comparison purposes, the obtained density values  $\rho_{\text{meas}}$  were related to a reference density of  $\rho_{\text{ref}} = 2.66 \text{ g/cm}^3$ , which is a manufacturer specification given in the supplier powder inspection certificate for AlSi10Mg. The determined comparative densities in terms of  $\rho_{\text{meas}}/\rho_{\text{ref}}$  are presented in Fig. 8. Most of the test specimens reached the reference value and those which did not, still reached relative densities above 99.5%. This is in line with results obtained by Kempen et al. [35], where relative densities between 98% and 100% were reported as well. It must be noted, that the uncertainty for this inspection method (interval of reproducibility =  $0.03 \text{ g/cm}^3$ ) was high compared to the difference between the results (highest value  $2.710 \text{ g/cm}^3$  and lowest value  $2.650 \text{ g/cm}^3$ ).

Furthermore, it appeared, that in the foremost part of the building area test specimens with lower densities and consequently more voids were manufactured. However, small air bubbles are known to adhere to the rough surfaces of AM test specimens [10], leading to the indication of a systematic failure during the measurement process of the AB-specimens.

### 3.4 Static tensile properties

The static tensile properties of all 60 S-specimens were derived according to DIN EN ISO 6892-1. The tests were conducted on a ZwickRoell universal testing machine with a 500 kN load cell.

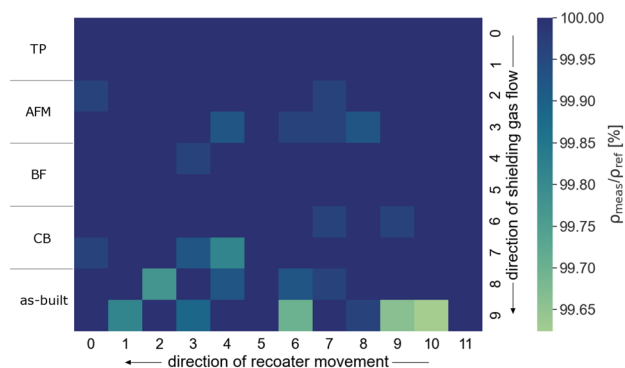


**Fig. 8** Distribution of the relative density over the build tray for various surface finish conditions



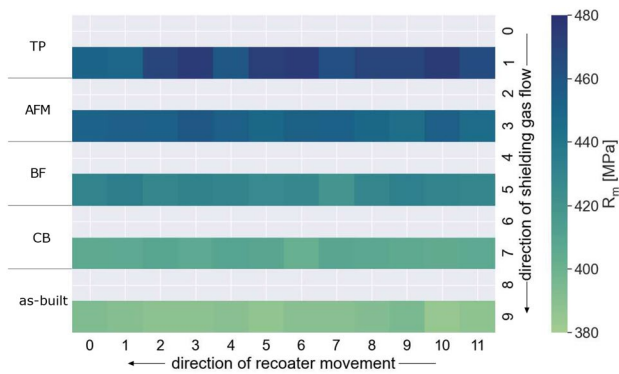


**Fig. 9** Ultimate tensile strength distribution on the platform for specimens in various surface finish conditions, data as measured

**Table 7** Results for the ultimate tensile strength  $R_m$ , the yield strength  $R_{p0.2}$  and the Young's modulus  $E$ , means per post-process category

Row	$R_m$ (MPa)	$R_{p0.2}$ (MPa)	$E$ (GPa)	Finish
0	$466 \pm 5$	$274 \pm 2$	$73.4 \pm 1.5$	TP
2	$452 \pm 2$	$270 \pm 1$	$72.6 \pm 1.4$	AFM
4	$430 \pm 1$	$268 \pm 1$	$73.9 \pm 2.3$	BF
6	$407 \pm 1$	$262 \pm 1$	$71.4 \pm 2.4$	CB
8	$390 \pm 2$	$247 \pm 1$	$66.9 \pm 1.2$	As-built

### 3.4.1 Ultimate tensile strength

The results of the ultimate tensile strength  $R_m$  are presented in Fig. 9. No assessment of systematic uncertainty is given, because the methods described in DIN EN ISO 6892-1 account for those and an additional estimation is only of informative nature [36]. Therefore, the statistical uncertainty for a 95% confidence interval, as explained in the beginning of this chapter, is stated in Table 7, which summarises the results.

The derived ultimate tensile strengths varied considerably with the final surface condition. This was remarkable since, in contrast to the fatigue properties, the tensile strength is known to be only slightly dependent on the surface quality [37]. The difference of up to 20% between the finish categories were unlikely to result solely from stress concentration and crack growth in the surface layers of the parts. DIN EN ISO 6892-1 generally states that the surface of the test specimens must be in such a condition, that it does not influence the result. However this statement is not specified any further. The ASTM Standard E8/E8M-21 [38] states that attention should be given while testing machined specimens with rough surfaces, since those can affect the properties to be measured, especially the variability of the test results, which is also discussed by du Plessis et al. [39]. The powder

manufacturer states that an  $R_m$  of 460 MPa was derived according to ISO 6892-1, B10 for AlSi10Mg with samples generally in an as manufactured state, but which were machined nevertheless [40]. Other references derived  $R_m$  for as-built specimens that were in the order of the results shown in this study, for example  $396 \pm 8$  MPa [10],  $377 \pm 5$  MPa [22] or 386 MPa [41].

An increase of  $R_m$  and elongation at break was also observed by Boschetto et al. for barrel finished Ti6Al4V test specimens [42] and by Nalli et al. [43]. The latter argued that the surface roughness acted as a series of superficial defects, causing premature fractures. Furthermore, a tendency of lower  $R_m$  for as-built specimens than finished ones manufactured by Selective Electron Beam Melting from Ti-6Al-4V was also observed by Sun et al. [11]. They explained this effect with near-surface defects (lack of fusion and surface grooves), which favoured crack initiation and propagation under low applied tensile stresses.

Another approach to explain the observed effect is to consider the reduced load-bearing cross-sectional area for specimens with high surface roughness. The tensile strength is calculated from the maximum force  $F_{max}$  applied in the tensile test and the specimens' cross sections, which are derived from the specimens' diameter  $d_m$ :

$$R_m = \frac{F_{max}}{\frac{\pi}{4} d_m^2}. \quad (2)$$

The diameter is usually determined with a caliper gauge or an outside micrometre. With  $Rz$  values of up to 220  $\mu\text{m}$  and diameters in the order of 5 mm, a significant part of the measured dimension are surface roughness peaks or valleys. Therefore, the specimens' bearing cross-sectional areas have been overestimated using an external diameter measurement method. To apply an adequate adaption, the doubled  $Rz$  values were subtracted from the measured diameters:

$$d_r = d_m - 2 \cdot Rz. \quad (3)$$

Figure 10 visualises the described approach. A similar procedure was followed by Mehta et al. while investigating the compressive strength of thin 326 L stainless steel shells [12]. As described in Sect. 3.1.3, the values of  $Rz_{opt}$  are considered to be reliable measures of the specimens' surface roughness.

For an adaption in this study, the arithmetic means of the optically measured  $Rz$  values per surface treatment category were used to apply the method. The TP-specimens were used as reference, so a  $\Delta Rz$  as difference between the mean  $Rz_{TP}$  and the  $Rz$  values of the other finish categories was calculated and applied to the measured external diameters of each individual test specimen. The results of the applied adaptations are summarised in Table 8.

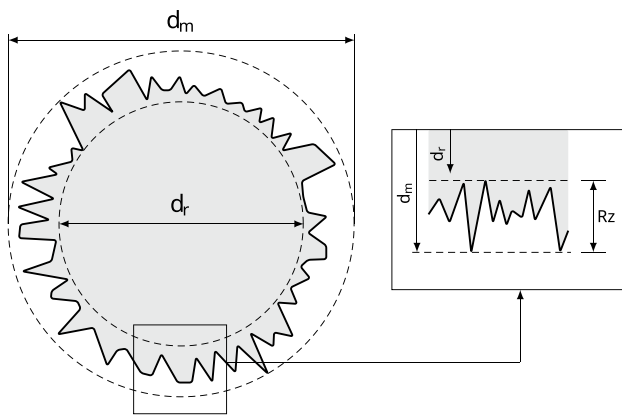


**Fig. 10** Schematic sketch of a measured diameter  $d_m$  and that of a bearing cross section  $d_r$  reduced by a high surface roughness  $R_z$

The adapting measures led to reduced differences between the tensile strengths across the five surface finish categories. However, it is highly probable that the previously described influences, like near-surface defects and notch effects, affected these values. A significant part of the defect afflicted surface was removed from test specimens treated with AFM and therefore, were in line with the reference (TP) after the adaption. It is important to note, that the optical measurement could only be performed on a smaller portion of the samples, hence the combined uncertainty as given in Table 8 is comparably high, especially for the TP category. Figure 11 shows the distribution of the adapted tensile strengths over the build tray.

### 3.4.2 Yield strength

The analysis of the derived yield strengths  $R_{p0.2}$  showed a similar dependency on the applied finish, but less pronounced than on the ultimate tensile strength. The result is shown in Fig. 12 and summarised in Table 7 for each category of surface condition.

The values, which have been determined in this study, are higher than those given by the manufacturer of 230 MPa (30  $\mu\text{m}$  layer thickness) or 240 MPa (60  $\mu\text{m}$  layer thickness) respectively for machined (turned) samples [40], but are in

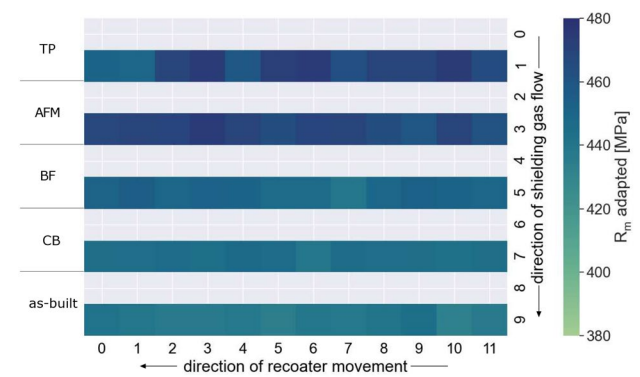


**Fig. 11** Ultimate tensile strength distribution of post-processed specimens over the build tray, data adapted for reduced bearing cross section using  $R_z$

line with other research groups like Silvestri et al. (250 MPa) [41].

Since the yield strength according to DIN EN ISO 6892-1 is derived from the linear-elastic section of the force–strain curve, the values have been adapted for the reduced bearing cross section as described previously in Sect. 3.4.1. The results are given in Fig. 13 and Table 9. The adapting measures led to a reduction of the differences between the yield strengths across the surface finish categories, especially for the as-built condition compared to the reference.

### 3.4.3 Young's modulus

The Young's modulus is derived from the linear-elastic section of the stress–strain curve. According to the standard DIN EN ISO 6892-1, the relevant part of the stress–strain curve, through which a linear regression will be fitted, should be chosen based on the yield strength. Despite the fact that the Young's modulus  $E$  is derived from the same stress–strain data like the other static tensile properties, the initial results (without adaption for the cross-sectional area) appeared to be less dependent on the applied surface finish method, apart from the as-built specimens. The results per treatment category are summarised in table 7 and are displayed for each individual specimen in figure 14. In general, the results were comparable to other studies with

**Table 8** Results for the adaption of measured  $R_m$  values for the mean roughness depths  $R_z$  for each category of surface treatment, arithmetic means per finish category given

	TP	AFM	BF	CB	S-built
$\bar{R}_m$ (MPa)	$466 \pm 5$	$452 \pm 2$	$430 \pm 1$	$407 \pm 1$	$390 \pm 2$
$\Delta\bar{R}_m$ (%)	Reference	3.0	7.8	12.7	16.4
$\bar{R}_{z,opt}$ ( $\mu\text{m}$ )	$24.3 \pm 10.8$	$67.0 \pm 7.7$	$84.6 \pm 4.4$	$146.8 \pm 4.2$	$171.9 \pm 7.2$
$\bar{R}_{m,adap}$ (MPa)	$466 \pm 5$	$468 \pm 2$	$450 \pm 2$	$445 \pm 1$	$439 \pm 2$
$\Delta\bar{R}_{m,adap}$ (%)	Reference	0.3	3.4	4.4	5.9

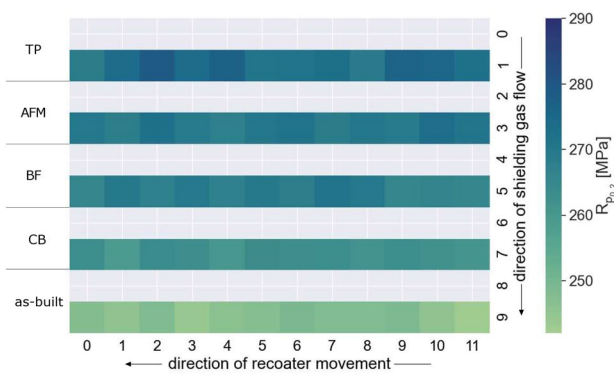


**Fig. 12** Yield strength distribution on the build tray for surface treated specimens, data as measured

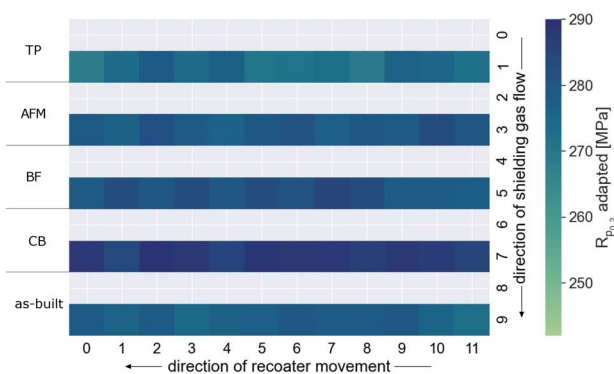


**Fig. 13** Yield strength distribution of post-processed specimens over the build tray, data adapted for reduced bearing cross section using  $R_z$

AlSi10Mg specimens, e.g.  $68 \pm 3$  GPa [10], 67 GPa [41] or  $74.8 \pm 1.0$  GPa [22].

However, the Young’s modulus corresponding to the as-built test specimens deviated notably from the other specimens. It is important to notice, that the Young’s modulus quantifies the physical behaviour of the material itself. This said, it should not be dependent on the surface condition to the extent observed in the derived data. This seconds the geometric and metrological influences on the determined tensile strength explained in Sect. 3.4.1. Therefore, an adaption as described in 3.4.1 has been applied. The results are

displayed in figure 15 and Table 10. By accounting for the reduced load-bearing cross-section, the comparatively high difference between the AB- and TP-specimens has been decreased.

When comparing the stress–strain curves for the TP- and the AB-specimens, see Fig. 16, one finds that the last-mentioned have a smaller linear-elastic section than the others. The extended elastic–plastic section can be explained by micro-scale plastic deformation due to notch effects, which occurs before the material experiences global plastic deformation. This, of course, has an influence on the Young’s modulus data, since the procedure to determine this value is based on the linear-elastic section of the stress–strain curve.

### 3.5 Fatigue properties

In general, it is known that different surface treatments have a significant impact on material fatigue properties due to the resulting variable surface roughness [38, 39]. The objective in this study was the investigation of the fatigue behaviour and the determination of the scatter of the results for different surface treatments in particular.

The testing has been carried out according to DIN EN 6072 on a 20 kN horizontal pulsator PPV2 by Carl Schenk Maschinenfabrik GmbH. The limit for runout specimens was set to be 3 million load cycles. The results are shown in Fig. 17. Initially it was planned to test all specimens at two load levels of 60 MPa and 100 MPa. During the tests it became obvious, that the CB-specimens would have been mostly runout specimens and hence, information to their fatigue behaviour would have been lost. For this reason, the decision was made to test these specimens on higher load levels to generate meaningful data. In total eight specimens were runouts: two CB-specimens on 100 MPa; one AFM-specimen on 60 MPa and four TP-specimens on 60 MPa.

Despite a rather high surface roughness, the CB-specimens showed an increased fatigue resistance at a load level of 100 MPa, but also a high scatter, even if compared to the TP-specimens. This observation results from two effects. First, the higher fatigue resistance is a consequence of the blasting process. Upon the impact of the blasting particles, the specimen surfaces experience a slight plastic deformation. This introduces compression stresses in the outer layer

**Table 9** Results for the adaption of measured  $R_{p0.2}$  values for the mean roughness depths  $R_z$  for each category of surface treatment, arithmetic means per finish category given

	TP	AFM	BF	CB	As-built
$\bar{R}_{p0.2}$ (MPa)	$274 \pm 2$	$270 \pm 1$	$268 \pm 1$	$262 \pm 1$	$247 \pm 1$
$\Delta \bar{R}_{p0.2}$ (%)	Reference	1.2	2.0	4.1	9.8
$\bar{R}_{z_{opt}}$ ( $\mu\text{m}$ )	$24.3 \pm 10.8$	$67.0 \pm 7.7$	$84.6 \pm 4.4$	$146.8 \pm 4.2$	$171.9 \pm 7.2$
$\bar{R}_{p0.2,adap}$ (MPa)	$274 \pm 2$	$280 \pm 1$	$281 \pm 1$	$287 \pm 1$	$278 \pm 1$
$\Delta \bar{R}_{p0.2,adap}$ (%)	Reference	2.2	2.7	5.0	1.5

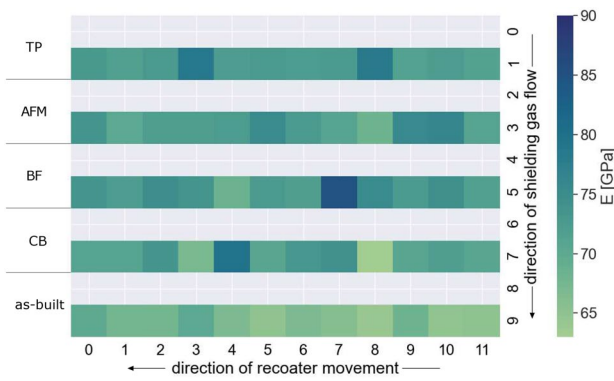


**Fig. 14** Young’s modulus distribution over the build tray for various surface finish conditions, data as measured data

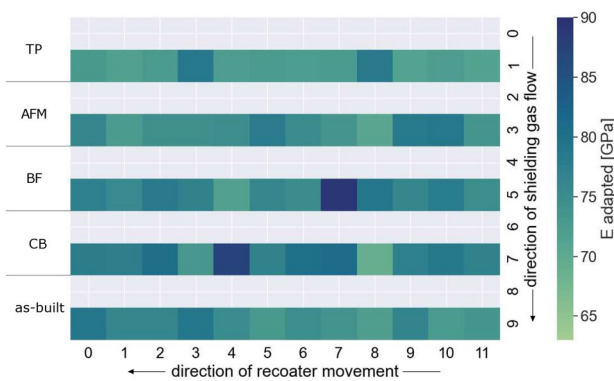


**Fig. 15** Young’s modulus distribution of post-processed specimens over the build tray, data adapted for reduced bearing cross section using *Rz*

of the surface, which counteract the formation of cracks during cyclic tension loading [15]. Second, during centrifugal blasting, the particles were ejected in various directions, which causes the impact direction and energy of the particles to vary significantly. This leads to inhomogeneous surface properties, which in turn affect the scattering of the fatigue properties. The surface treatment processes BF, AFM and TP are primarily erosive processes. They did not influence the stress state in the specimen surfaces to a significant amount. Therefore, the fatigue values of these specimens

were lower than those of the CB-specimens and did not scatter as much.

The lowest number of cycles was achieved by the AB-specimens. The fatigue properties of those were dominated by the influence of the surface roughness and hence, were improved across the finish categories with decreasing surface roughness. However, these samples showed only a slight scatter. All surface finishes increased the scatter of the data, but improved the fatigue properties as well.

### 4 Conclusions

The present study aimed to increase the understanding of the influence of different surface treatment processes on part quality as well as mechanical properties of additive manufactured metallic parts. Therefore, the impact of four different surface treatment methods on the properties of AISi10Mg test specimens has been investigated. Generally, different surface finish methods are suitable for additive manufactured parts in an aerospace application, depending on the intended location of service and the applied loads.

Regarding the achieved surface quality in terms of surface roughness, strong differences between the surface treatment methods have been observed.

It was confirmed, that the tactile and the optical surface measuring method provided comparable results for the determination of *Ra* and *Rz* when measuring the surface of identical specimen areas. However, an essential precondition is the consistency of the selected parameters for the evaluation of the acquired profiles. Consequently, if *Ra* and *Rz* are a measure of surface quality for a component, there must be a surface available, which allows for correct measurement in terms of length and flatness. This is a challenge for weight-optimised, often bionic aircraft components, especially when considering, that the surface roughness depends on part geometry and the orientation of the parts’ surfaces in the build space.

Furthermore, one of the main findings of the conducted study was the dependency of the determined material strengths on the specimens’ surface roughness. This was foreseeable for dynamic load cases, but less expected for static tensile tests. Analysing the initial test data, one finds

**Table 10** Results for the adaption of measured *E* values for the mean roughness depths *Rz* for each category of surface treatment, arithmetic means per finish category given

	TP	AFM	BF	CB	As-built
$\bar{E}$ (GPa)	73.4 ± 1.5	72.6 ± 1.4	73.9 ± 2.3	71.4 ± 2.4	66.9 ± 1.2
$\Delta\bar{E}$ (%)	Reference	1.0	0.8	2.6	8.8
$\bar{Rz}_{opt}$ (µm)	24.3 ± 10.8	67.0 ± 7.7	84.6 ± 4.4	146.8 ± 4.2	171.9 ± 7.2
$\bar{E}_{adap}$ (GPa)	73.4 ± 1.5	75.1 ± 1.4	77.4 ± 2.4	78.1 ± 2.5	75.3 ± 1.3
$\Delta\bar{E}_{adap}$ (%)	Reference	2.4	5.5	6.5	2.6

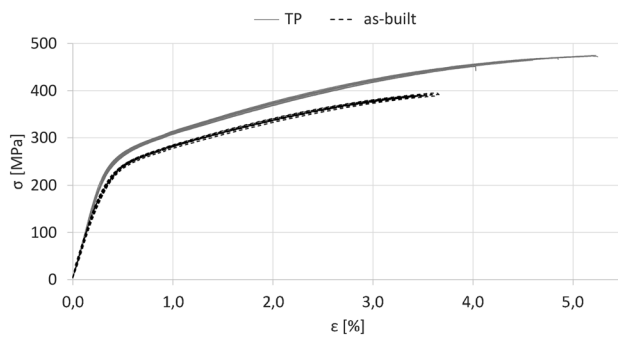


**Fig. 16** Stress–strain curves of twelve as-built and twelve TP-specimens, data as measured

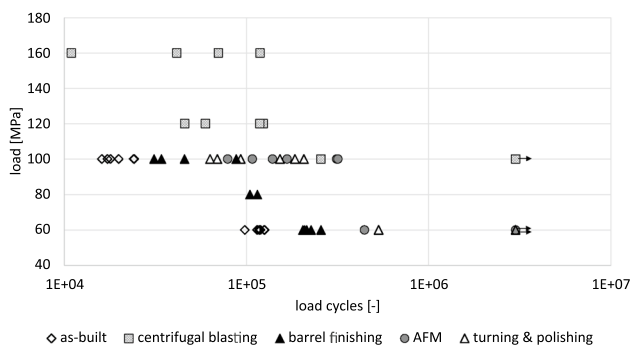


**Fig. 17** Load cycles on multiple loads for different post-processing methods, arrows indicate runouts, data as measured

that yield strength and ultimate tensile strength vary considerably with the test specimens' surface roughness. The Young's modulus derived from the as-built specimens deviated also significantly from those determined from the surface treated specimens. But linking the deviation to a mechanical influence on the tensile behaviour would be misleading, since the same material with an equal microstructure must show the same linear-elastic behaviour. This seconds the described assumption of meteorological effects on the standardised measurement and analysis of tensile tests. As a result of the very high surface roughness, the load-bearing cross sections of AM parts are significantly overestimated, leading to reduced mechanical properties. In this context, a method to adapt static tensile properties to surface roughness was suggested in this study.

Geometrically identical specimens manufactured with the same type of powder on the same machine might show differing strength properties, if one specimen group is processed with a set A of process parameters and a second group with a parameter set B.

If set A produces specimens with an increased surface roughness compared to set B, which are dependent on the manufacturing parameters as well [44, 45], the bearing

cross section determined by external measurement would be overestimated for the A-specimens. If those cross sections are then used to calculate the stress–strain data, one would obtain reduced tensile properties, except the Young's modulus, from set A compared to set B. These differences would not solely originate from a changed microstructure due to the differing process parameters, but also from the different as-built surface conditions.

In conclusion, to determine an AM parts' strength properties, a statement regarding surface quality or the applied post-processing steps appears to be necessary.

It was also confirmed, that all evaluated methods of surface treatment increased the fatigue resistance of the AlSi10Mg test specimens. Despite the comparably high surface roughness, centrifugal blasting achieved the highest improvement on this property, while simultaneously increasing the scatter significantly.

The relative density of all examined test specimens was above 99.5%. In addition, the surface hardness appeared to be evenly distributed across the build tray, but there has been a slight tendency of variance between the two investigated types of test specimens.

Furthermore, there was no indication of any influence of the specimens' position on the build tray across all measured properties. The results along the recoater axis were evenly distributed. However, it must be considered, that a similar statement cannot be made along the transverse axis of the shielding gas flow, since the surface finishes were varied along this axis. Further work is currently in progress to investigate the influence of such parameters, which can only be determined over multiple build cycles, like the influence of powder characteristics and the position on the build tray during the process.

With reference to the qualification of parts in the aviation industry one can conclude: If material properties are derived from as-built specimens and this data is used to design or optimise a part which undergoes surface treatment, the dimensions of this part would be overestimated. On the other hand, a part in as-built condition would fail, if the design was based on material characteristics investigated with surface treated specimens. Either way, to design safe parts for aerospace applications, which need to be optimised regarding their mass to strength ratio, these dependencies need to be taken into consideration.

**Acknowledgements** The research leading to these results received funding from the Federal Ministry for Economic Affairs and Climate Action under Grant Agreement No 20D1925E on the basis of a decision by the German Bundestag. The responsibility for the content of this publication lies with the authors.

**Author contributions** Conceptualization: CR; methodology: CR, GN, WG, TS and FH; data collection: TS, GG and RT; formal analysis and investigation: CR and GN; writing—original draft preparation: CR and GN (section surface roughness); writing—review and editing:

GN, WG, FH, GG, RT, TS and JH; funding acquisition: FH and JM; supervision: JM.

**Funding** Open Access funding enabled and organized by Projekt DEAL. Open Access Funding was generously granted by the Publication Fund of the TU Dresden within the scope of the Projekt DEAL.

**Data availability** Data sets generated during the current study are available from the corresponding author on reasonable request.

## Declarations

**Conflict of interest** There are no potential conflicts of interest for the authors to disclose. There are no financial interests to record, and all co-authors have seen and agreed to the contents of the work. We certify that the submission is unique and that it is not currently under consideration by another publisher.

**Open Access** This article is licensed under a Creative Commons Attribution 4.0 International License, which permits use, sharing, adaptation, distribution and reproduction in any medium or format, as long as you give appropriate credit to the original author(s) and the source, provide a link to the Creative Commons licence, and indicate if changes were made. The images or other third party material in this article are included in the article's Creative Commons licence, unless indicated otherwise in a credit line to the material. If material is not included in the article's Creative Commons licence and your intended use is not permitted by statutory regulation or exceeds the permitted use, you will need to obtain permission directly from the copyright holder. To view a copy of this licence, visit <http://creativecommons.org/licenses/by/4.0/>.

## References

1. Airbus Helicopters: Airbus Helicopters to start large-scale printing of A350 XWB components. <https://www.airbus.com/en/newsroom/press-releases/2018-09-airbus-helicopters-to-start-large-scale-printing-of-a350-xwb>. Accessed 6 Jan 2023 (2018)
2. Liebherr: World Premier: First Ever 3D Printed Primary Flight Control Component from Liebherr-Aerospace Flown on an Airbus Aircraft. <https://www.liebherr.com/en/ind/latest-news/news-press-releases/detail/world-premier-first-ever-3d-printed-primary-flight-control-component-from-liebherr-aerospace-flown-on-an-airbus-aircraft.html>. Accessed 6 Jan 2023 (2017)
3. EASA: Certification Memorandum Additive Manufacturing. Issue 03. <https://www.easa.europa.eu/en/documentlibrary/product-certification-consultations/final-certification-memorandum-ref-cm-s-008>. Accessed 12 Dec 2022(2021)
4. Kruth, J.-P., Badrossamay, M., Yasa, E., Deckers, J., Thijs, L., Humbeeck, J.V.: Part and material properties in selective laser melting of metals. In: 16th International Symposium on Electromachining (ISEM XVI), Shanghai, China (2010)
5. Campanelli, S.L., Contuzzi, N., Angelastro, A., Ludovico, A.D.: Capabilities and Performances of the Selective Laser Melting Process, New Trends in Technologies: Devices, Computer, Communication and Industrial Systems. InTech, Rijeka (2010). ISBN: 978-953-307-212-8. <http://www.intechopen.com/books/new-trends-in-technologies-devices-computer-communication-and-industrial-systems/capabilities-and-performances-of-the-selective-laser-melting-process>
6. Kim, E.-J., Lee, C.-M., Kim, D.-H.: The effect of post-processing operations on mechanical characteristics of 304L stainless steel fabricated using laser additive manufacturing. *J. Mater. Res. Technol.* **15**, 1370–1381 (2021). <https://doi.org/10.1016/j.jmrt.2021.08.142>
7. Kaynak, Y., Kitay, O.: The effect of post-processing operations on surface characteristics of 316L stainless steel produced by selective laser melting. *Addit. Manuf.* **26**, 84–93 (2019). <https://doi.org/10.1016/j.addma.2018.12.021>
8. Tradowsky, U., White, J., Ward, R.M., Read, N., Reimers, W., Attallah, M.M.: Selective laser melting of AlSi10Mg: influence of post-processing on the microstructural and tensile properties development. *Mater. Des.* **105**, 212–222 (2016). <https://doi.org/10.1016/j.matdes.2016.05.066>
9. Hitzler, L., Janousch, C., Schanz, J., Merkel, M., Heine, B., Mack, F., Hall, W., Öchsner, A.: Direction and location dependency of selective laser melted AlSi10Mg specimens. *J. Mater. Process. Technol.* **243**, 48–61 (2017). <https://doi.org/10.1016/j.jmatprotec.2016.11.029>
10. Kempen, K., Thijs, L., Humbeeck, J.V., Kruth, J.-P.: Mechanical properties of AlSi10Mg produced by selective laser melting. *Phys. Procedia* **39**, 439–446 (2012). <https://doi.org/10.1016/j.phpro.2012.10.059>
11. Sun, Y.Y., Gulizia, S., Oh, C.H., Fraser, D., Leary, M., Yang, Y.F., Qian, M.: The influence of as-built surface conditions on mechanical properties of Ti–6Al–4V additively manufactured by selective electron beam melting. *J. Miner. Met. Mater. Soc. (TMS)* **68**(3), 791–798 (2016). <https://doi.org/10.1007/s11837-015-1768-y>
12. Mehta, B., Hryha, E., Nyborg, L., Tholence, F., Johansson, E.: Effect of surface sandblasting and turning on compressive strength of thin 316l stainless steel shells produced by laser powder bed fusion. *MDPI Metals* **11**(7), 1070 (2021). <https://doi.org/10.3390/met11071070>
13. Rauch, M., Hascoet, J.-Y.: A comparison of post-processing techniques for additive manufacturing components. *Procedia CIRP* **108**, 442–447 (2022). <https://doi.org/10.1016/j.procir.2022.03.069>
14. Peng, X., Kong, L., Fuh, J.Y.H., Wang, H.: A review of post-processing technologies in additive manufacturing. *J. Manuf. Mater. Process.* **5**(2), 38 (2021). <https://doi.org/10.3390/jmmp5020038>
15. Khan, H.M., Karabulut, Y., Kitay, O., Kaynak, Y., Jawahir, I.S.: Influence of the post-processing operations on surface integrity of metal components produced by laser powder bed fusion additive manufacturing: a review. *Mach. Sci. Technol.* **25**(1), 118–176 (2021). <https://doi.org/10.1080/10910344.2020.1855649>
16. Limbasiya, N., Jain, A., Soni, H., Wankhede, V., Krolczyk, G., Sahlot, P.: A comprehensive review on the effect of process parameters and post-process treatments on microstructure and mechanical properties of selective laser melting of AlSi10Mg. *J. Mater. Res. Technol.* **21**, 1141–1176 (2022). <https://doi.org/10.1016/j.jmrt.2022.09.092>
17. Pal, R., Basak, A.: Linking powder properties, printing parameters, post-processing methods, and fatigue properties in additive manufacturing of AlSi10Mg. *Alloys* **1**(2), 149–179 (2022). <https://doi.org/10.3390/alloys1020010>
18. Calignano, F., Galati, M., Iuliano, L.: A metal powder bed fusion process in industry: qualification considerations. *MDPI Machines* **7**(4), 72 (2019). <https://doi.org/10.3390/machines7040072>
19. Vock, S., Klöden, B., Kirchner, A., Weißgärber, T., Kieback, B.: Powders for powder bed fusion: a review. *Prog. Addit. Manuf.* **4**(4), 383–397 (2019). <https://doi.org/10.1007/s40964-019-00078-6>
20. Boschetto, A., Bottini, L., Macera, L., Veniali, F.: Post-processing of complex SLM parts by Barrel finishing. *Appl. Sci.* **10**(4), 1382 (2020). <https://doi.org/10.3390/app10041382>
21. Bremerstein, T., Potthoff, A., Michaelis, A., Schmiedel, C., Uhlmann, E., Blug, B., Amann, T.: Wear of abrasive media and its effect on abrasive flow machining results. *Wear* **342–343**, 44–51 (2015). <https://doi.org/10.1016/j.wear.2015.08.013>

22. Sert, E., Hitzler, L., Hafenstein, S., Merkel, M., Werner, E., Öchsner, A.: Tensile and compressive behaviour of additively manufactured AlSi10Mg samples. *Prog. Addit. Manuf.* **5**(3), 305–313 (2020). <https://doi.org/10.1007/s40964-020-00131-9>
23. Ponnusamy, P., Rashid, R.A.R., Masood, S.H., Ruan, D., Palanisamy, S.: Mechanical properties of SLM-printed aluminium alloys: a review. *MDPI Materials* **13**(19), 4301 (2020). <https://doi.org/10.3390/ma13194301>
24. Mfusi, B.J., Mathe, N.R., Tshabalala, L.C., Popoola, P.A.: The effect of stress relief on the mechanical and fatigue properties of additively manufactured AlSi10Mg parts. *MDPI Metals* **9**(11), 1216 (2019). <https://doi.org/10.3390/met9111216>
25. JCGM 100: Evaluation of measurement data—guide to the expression of uncertainty in measurement. BIPM/IEC/IFCC/ILAC/ISO/IUPAC/IUPAP/OIML (2008)
26. Wycisk, E., Emmelmann, C., Siddique, S., Walther, F.: High cycle fatigue (HCF) performance of Ti–6Al–4V alloy processed by selective laser melting. *Adv. Mater. Res.* **816–817**, 134–139 (2013). <https://doi.org/10.4028/www.scientific.net/amr.816-817.134>
27. Li, B.-Q., Li, Z., Bai, P., Liu, B., Kuai, Z.: Research on surface roughness of AlSi10Mg parts fabricated by laser powder bed fusion. *MDPI Metals* **8**(7), 524 (2018). <https://doi.org/10.3390/met8070524>
28. Conroy, M., Armstrong, J.: A comparison of surface metrology techniques. *J. Phys. Conf. Ser.* **13**(1), 458 (2005). <https://doi.org/10.1088/1742-6596/13/1/106>
29. Piska, M., Metelkova, J.: On the comparison of contact and non-contact evaluations of a machined surface. *MM Sci. J.* **2**, 476–479 (2014). [https://doi.org/10.17973/mmsj.2014\\_06\\_201408](https://doi.org/10.17973/mmsj.2014_06_201408)
30. Bernevig-Sava, M.A., Stamate, C., Lohan, N., Baci, A.M., Postolache, I., Baci, C., Baci, E.: Considerations on the surface roughness of SLM processed metal parts and the effects of subsequent sandblasting. *IOP Conf. Ser. Mater. Sci. Eng.* **572**(1), 012071 (2019). <https://doi.org/10.1088/1757-899x/572/1/012071>
31. Cheng, F., Fu, S.W., Leong, Y.S.: Research on optical measurement for additive manufacturing surfaces. In: *Proceedings of SPIE—The International Society for Optical Engineering*, vol. 10250 (2017). <https://doi.org/10.1117/12.2266653>
32. Marchese, G., Aversa, A., Lorusso, M., Manfredi, D., Calignano, F., Lombardi, M., Biamino, S., Pavese, M.: Development and characterisation of aluminium matrix nanocomposites AlSi10Mg/MgAl<sub>2</sub>O<sub>4</sub> by laser powder bed fusion. *MDPI Metals* **8**(3), 175 (2018). <https://doi.org/10.3390/met8030175>
33. Padovano, E., Badini, C., Pantarelli, A., Gili, F., D’Aiuto, F.: A comparative study of the effects of thermal treatments on AlSi10Mg produced by laser powder bed fusion. *J. Alloy. Compd.* **831**, 154822 (2020). <https://doi.org/10.1016/j.jallcom.2020.154822>
34. DIN EN ISO 3369:2010: Undurchlässige Sintermetallwerkstoffe und Hartmetalle—Ermittlung der Dichte. DIN Deutsches Institut für Normung e.V., Berlin (2010)
35. Kempen, K., Thijs, L., Humbeeck, J.V., Kruth, J.-P.: Processing AlSi10Mg by selective laser melting: parameter optimisation and material characterisation. *Mater. Sci. Technol.* **31**(8), 917–923 (2014). <https://doi.org/10.1179/1743284714y.0000000702>
36. DIN EN ISO 6892-1: Metallische Werkstoffe—Zugversuch—Teil 1: Prüfverfahren Bei Raumtemperatur. DIN Deutsches Institut für Normung e.V., Berlin (2020)
37. Läßle, V.: Einführung in die Festigkeitslehre. Springer, Wiesbaden (2016)
38. ASTM International: E8/E8M-21: Standard Test Methods for Tension Testing of Metallic Materials (2021). [https://doi.org/10.1520/e0008\\_e0008m-21](https://doi.org/10.1520/e0008_e0008m-21)
39. du Plessis, A., Yadroitseva, I., Yadroitsev, I.: Effects of defects on mechanical properties in metal additive manufacturing: a review focusing on X-ray tomography insights. *Mater. Des.* **187**, 108385 (2020). <https://doi.org/10.1016/j.matdes.2019.108385>
40. EOS GmbH: EOS Aluminium AlSi10Mg—Material Data Sheet. [https://www.eos.info/03\\_system-related-assets/material-related-content/metal-materials-and-examples/metal-material-datasheet/aluminium/material\\_datasheet\\_eos\\_aluminium-alsi10mg\\_en\\_web.pdf](https://www.eos.info/03_system-related-assets/material-related-content/metal-materials-and-examples/metal-material-datasheet/aluminium/material_datasheet_eos_aluminium-alsi10mg_en_web.pdf). Accessed 21 Dec 2022 (2022)
41. Silvestri, A.T., Astarita, A., Hassanin, A.E., Manzo, A., Iannuzzo, U., Iannuzzo, G., Rosa, V.D., Acerra, F., Squillace, A.: Assessment of the mechanical properties of AlSi10Mg parts produced through selective laser melting under different conditions. *Procedia Manuf.* **47**, 1058–1064 (2020). <https://doi.org/10.1016/j.promfg.2020.04.115>
42. Boschetto, A., Bottini, L., Veniali, F.: Surface roughness and radiusing of Ti6Al4V selective laser melting-manufactured parts conditioned by barrel finishing. *Int. J. Adv. Manuf. Technol.* **94**(5–8), 2773–2790 (2017). <https://doi.org/10.1007/s00170-017-1059-6>
43. Nalli, F., Bottini, L., Boschetto, A., Cortese, L., Veniali, F.: Effect of industrial heat treatment and Barrel finishing on the mechanical performance of Ti6Al4V processed by selective laser melting. *Appl. Sci.* **10**(7), 2280 (2020). <https://doi.org/10.3390/app10072280>
44. Whip, B., Sheridan, L., Gockel, J.: The effect of primary processing parameters on surface roughness in laser powder bed additive manufacturing. *Int. J. Adv. Manuf. Technol.* **103**, 4411–4422 (2019). <https://doi.org/10.1007/s00170-019-03716-z>
45. Fox, J.C., Moylan, S.P., Lane, B.M.: Effect of process parameters on the surface roughness of overhanging structures in laser powder bed fusion additive manufacturing. *Procedia CIRP* **45**, 131–134 (2016). <https://doi.org/10.1016/j.procir.2016.02.347>. (3rd CIRP Conference on Surface Integrity)

**Publisher's Note** Springer Nature remains neutral with regard to jurisdictional claims in published maps and institutional affiliations.